Follow us @BoneJointOpen

Freely available online OPEN ACCESS

BJO

GENERAL ORTHOPAEDICS

Near-infrared spectroscopy for structural bone assessment

A POTENTIAL POINT-OF-CARE TOOL

V. J. Sharma, J. A. Adegoke, I. O. Afara, K. Stok, E. Poon, C. L. Gordon, B. R. Wood, J. Raman

From Austin Hospital, Heidelberg Melbourne, Australia

Aims

Disorders of bone integrity carry a high global disease burden, frequently requiring intervention, but there is a paucity of methods capable of noninvasive real-time assessment. Here we show that miniaturized handheld near-infrared spectroscopy (NIRS) scans, operated via a smartphone, can assess structural human bone properties in under three seconds.

Methods

A hand-held NIR spectrometer was used to scan bone samples from 20 patients and predict: bone volume fraction (BV/TV); and trabecular (Tb) and cortical (Ct) thickness (Th), porosity (Po), and spacing (Sp).

Results

NIRS scans on both the inner (trabecular) surface or outer (cortical) surface accurately identified variations in bone collagen, water, mineral, and fat content, which then accurately predicted bone volume fraction (BV/TV, inner $R^2 = 0.91$, outer $R^2 = 0.83$), thickness (Tb.Th, inner $R^2 = 0.9$, outer $R^2 = 0.79$), and cortical thickness (Ct.Th, inner and outer both $R^2 = 0.90$). NIRS scans also had 100% classification accuracy in grading the quartile of bone thickness and quality.

Conclusion

We believe this is a fundamental step forward in creating an instrument capable of intraoperative real-time use.

Cite this article: *Bone Jt Open* 2023;4-4:250–261.

Keywords: Vibrational spectroscopy, Near infrared spectroscopy, Spectromics, Chemometrics, Bone evaluation

Introduction

Currently, there are no point-of-care non-disruptive surgical tools that can assess the structural properties of bone, despite bone fractures and degeneration being a leading indication for surgery worldwide,[1,2] and bone incisions being routinely required in a range of operations.[3-9] Instead, clinicians are reliant on assessments, which are crude and based on preoperative risk factors (e.g. age, sex, diabetes, obesity)[10,11] or intraoperative findings (e.g. feel of the bone, fracture, frailty, thickness). Imaging techniques, such as MRI, CT, and dual-energy X-ray absorptiometry scans,[12] are resource- and time-intensive, and have limited capacity to assess bone volume fraction, morphology, or material properties.[12] Intraoperative probes such as the DensiProbe (AO Foundation, Switzerland)[13,14] are invasive and disrupt the integrity of the bone.[13] Noninvasive instruments, such as BoneIndex (Finland), are based on ultrasound, and cannot assess microstructural properties. This has significant clinical ramifications because surgical reconstruction methods are not tailored to the structural properties of the patient's bone (e.g. using mismatched screws, rods, pins, or plates not suitable for poor quality bone; or inadequate reinforcement of weak bone during advanced operative techniques; distinction between fixation versus joint arthroplasty,

Correspondence should be sent to Jaishankar Raman; email: jairaman2462@gmail.com

doi: 10.1302/2633-1462.44.BJO-2023-0014.R1

Bone Jt Open 2023;4-4:250–261.

etc). These evaluations can impact an array of postoperative morbidity and mortality, including poor healing, malunion of bone, technical failure, infection, re-intervention, and mortality.[15–18]

Non-perturbative bone assessment techniques using vibrational spectroscopy (such as Raman), mid-infrared spectroscopy (MIR), and near-infrared spectroscopy form a promising technological platform to assess bone integrity non-destructively during surgical procedures. Raman spectroscopy and MIR have been used for bone quality assessment,[19–22] but have significant limitations. These include highly calibrated instrumentation, management of interference from fluorescence (Raman spectroscopy), poor penetration depth of MIR spectroscopy (< 10 μm into soft-tissue), and high cost. In contrast, scans using near infrared spectroscopy (NIRS) are rapid, penetrate deeper into biological tissues (0.5 to 5 mm wavelength dependent), and use economical instrumentation providing information on overtone and combination bands from macromolecular functional groups.[23,24] Existing studies have demonstrated the ability of NIRS scans to assess animal[24] and cadaveric human[25] connective tissues, and to predict the integrity of articular cartilage.[26,27] However, no study has adapted miniaturized NIRS scans for assessment of fresh human bone, which is an important need/requirement for intraoperative use. In this proof-of-principle study, we examined the capacity of NIRS scans for non-destructive, rapid characterization and prediction of human sternal bone structural properties, assessed and cross-validated via the gold-standard Micro-CT scans.

Methods

Human bone samples. Fresh bone samples were collected prospectively from 20 consecutive donors providing organs for transplantation between 25 January and 27 July 2021 from the Australian Donation and Transplantation Biobank in Victoria, Australia, as shown in Figure 1. Bone samples were acquired intraoperatively at the time of organ retrieval from the sternotomy incision. To best emulate in vivo surface geometry, bone rongeurs were used to excise a 10 mm × 10 mm adjacent to the incision. The samples were taken from the entire thickness of the sternum, and therefore encompassed both the outer (cortical) surface and inner (trabecular) content, with representative samples shown in Figure 1 and Supplementary Figure b. Samples were transported on ice with organs to the donor retrieval surgical team, and immediately stored in 2 ml Eppendorf tubes, snap-frozen in liquid nitrogen, and stored in cryogenic tanks at -80°C. Samples were thawed for subsequent analysis.

NIRS scans. We obtained a three-second point-of-care scan of bone samples using a miniaturized NIRS instrument (Neospectra Puck v1.0; Si-ware Systems, USA). The instrument contained a spectrometer size of 32 × 32 × 22 mm (weight 17 gm), allowing handheld use with direct application onto tissue. Spectra were collected using a computer using the inbuilt app software (SpectroMOST micro, v 1.0, NeoSpectra; Si-ware Systems). Scans were taken at a spectral resolution of 16 nm as previously described for biological samples.[24]

Micro-CT (gold standard). To establish baseline structural properties of the bone as the 'gold standard' for comparison,[28,29] all fresh samples were subjected to Micro-CT (μCT50; Scanco Medical AG, Switzerland) after NIRS assessment (Table I). Similar to medical CT scans, these scans use 3D reconstructions CT images to deduce structural properties of both the outside (cortical) and inside (trabecular) of bone, with bone volume fraction (BV/TV) used as a surrogate to assess the quality of bone (Supplementary Figure b). All samples were scanned in with a 0.5 mm artificial intelligence (AI) filter at an energy of 55 kVp, intensity of 145 μA, integration time of 200 ms, 6 × frame averaging, and a voxel (native) resolution of 10.3 μm. Two samples were placed side-by-side in a 34 mm vial. Following scanning, samples were returned to their sample vials and stored at -20°C. Following scanning, a constrained 3D Gaussian filter was used to partly suppress the noise in the volumes (sigma of 0.8 and support of one voxel), and mineralized tissue was segmented from soft-tissues with a global threshold (22.4% of the maximum greyscale value). Cortical and trabecular masks were created using a series of automated scripts, and morphometric parameters were determined in each compartment. Parameters determined in the trabecular bone include bone volume fraction (BV/TV), trabecular thickness (Tb. Th), trabecular spacing (Tb. Sp), and trabecular number (Tb. N). Cortical porosity (Ct. Po) and cortical thickness (Ct. Th) were assessed in the cortical volume.

Statistical analysis. Clinical data were collected and managed using Research Electronic Data Capture (REDCap) electronic data capture tools hosted at Australian Donation and Transplantation Biobank (ADTB) which is a secure, web-based software platform designed to support data capture for research studies. Analysis of clinical data was performed using Stata v15.0 (StataCorp, USA), with clinical variables reported as either counts with corresponding percentages, or medians with interquartile ranges (IQRs). Differences between sexes were assessed using paired *t*-test for proportions and Mann-Whitney U test for continuous variables. Correlations between micro-CT variables were carried out using linear regression analysis and reported as correlation coefficients and 95% confidence intervals (CIs).

We compared results from NIRS scans with the micro-CT gold standard as outlined in Figure 1. First, NIRS scans were analyzed using PLS toolbox (Eigenvector Research, USA), an extensive suite of machine-learning and statistical tools for advanced data analysis, which can

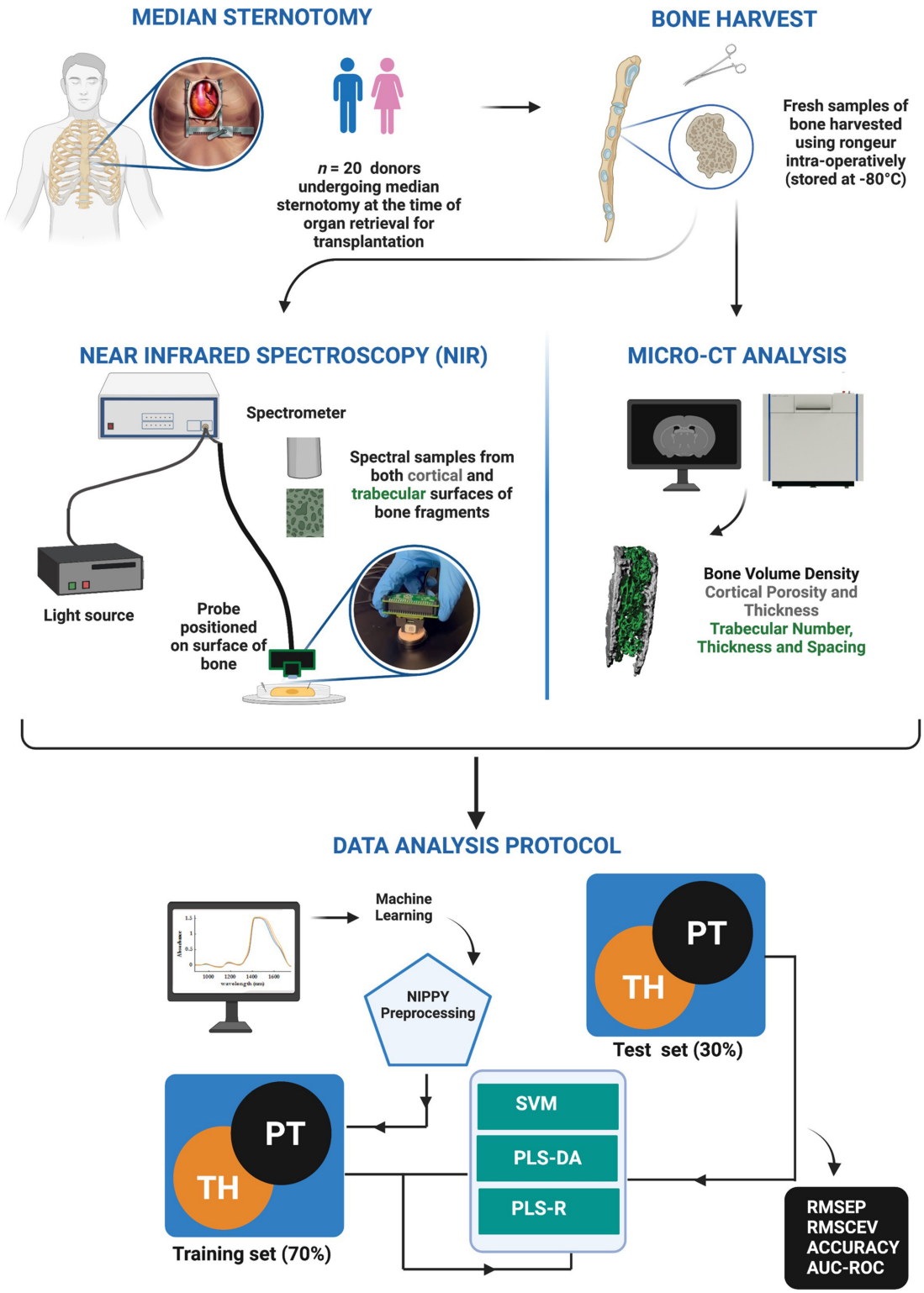

Fig. 1

Study design to evaluate human bone using near-infrared spectroscopy. A total of 20 donors undergoing median sternotomy at the time of organ retrieval for transplantation provided human bone samples. These were procured from the median sternotomy wound using bone rongeurs and stored at -80°C when not being analyzed. Bone samples were analyzed using a miniaturized near-infrared spectrometer so as to acquire spectra in two orientations: the cortical, PT (grey) and trabecular, TH (green) regions; and micro-CT. Parameters from Micro-CT were then correlated with NIR spectral data. Spectral data were pre-processed in 50 different ways using Nippy python module, and passed on for machine-learning. Abbreviations: AUC-ROC, area under curve of receiver operator characteristics; micro-CT, micro CT; NIR, near-infrared spectroscopy; PLS-DA, partial least square discrimination analysis; PLS-R, partial least square regression; RMSECV, root mean square of cross validation; RMSEP, root mean squared error of prediction; SVM, support vector machine.

Table I. Demographic distribution of donors from whom bone was obtained, stratified by sex.

Variable	All donors (n = 20)	Females (n = 8)	Male (n = 12)	p-value
Demographics				
Median age, yrs (IQR)	51 (35 to 59)	55 (46 to 59)	50 (42 to 58)	0.54*
Donation after brain death, n (%)	13 (65.0)	5 (62.5)	8 (66.7)	0.85†
Caucasian race, n (%)	17 (85.0)	7 (87.5)	10 (83.3)	0.80†
Median height, cm (IQR)	171.6 (164.5 to 180.5)	162.5 (157.5 to 166.5)	177.5 (174.5 to 181.5)	< 0.01*
Median weight, kg (IQR)	72.0 (64.5 to 93.0)	72.0 (60.0 to 92.5)	76.5 (65.5 to 97.0)	0.40*
Median BMI, kg/m^2 (IQR)	25.8 (22.3 to 30.5)	28.3 (23.0 to 34.4)	24.3 (22.3 to 27.3)	0.32*
Comorbidities, n (%)				
Asthma	2 (10.0)	2 (25.0)	0 (0.0)	0.07†
COPD	6 (30.0)	3 (37.5)	3 (25.0)	0.55†
Ischaemic heart disease	4 (20.0)	1 (12.5)	3 (25.0)	0.49†
Diabetes Mellitus	5 (15.0)	2 (25.0)	3 (25.0)	1.00†
Smoking history	18 (90.0)	7 (87.5)	11 (91.7)	0.76†
Osteoporosis	2 (10.0)	1 (12.5)	1 (8.3)	0.76†
Micro-CT				
Median cortical porosity, % (IQR)	8.38 (7.55 to 11.76)	8.38 (7.69 to 11.80)	8.38 (6.96 to 10.86)	1.00*
Median cortical thickness, mm (IQR)	0.40 (0.35 to 0.46)	0.41 (0.35 to 0.49)	0.40 (0.36 to 0.44)	0.59*
Median trabecular number, mm^{-1} (IQR)	1.92 (1.72 to 2.03)	1.91 (1.53 to 1.99)	1.95 (1.82 to 2.24)	0.24*
Median trabecular spacing, mm (IQR)	0.49 (0.45 to 0.56)	0.49 (0.47 to 0.62)	0.49 (0.43 to 0.52)	0.49*
Median trabecular thickness, mm (IQR)	0.12 (0.11 to 0.12)	0.12 (0.12 to 0.13)	0.11 (0.11 to 0.12)	0.02*
Median bone volume fraction, BV/TV (IQR)	0.18 (0.17 to 0.19)	0.18 (0.18 to 0.20)	0.17 (0.16 to 0.19)	0.49*
Median bone volume, % (IQR)‡	17.97 (16.54 to 19.19)	18.20 (17.57 to 19.54)	17.28 (16.30 to 19.19)	0.49*

*Paired *t*-test.
†Chi-squared test.
‡Bone volume (%) is a percentage representation of bone volume fraction.
BV, bone volume; COPD, chronic obstructive pulmonary disease; IQR, interquartile range; TV, total volume;

be operated within MATLAB environment (MathWorks, USA). In addition, Jupyter notebook (Project Jupyter, USA), an interactive web-based computing platform equipped with an extensive data analysis library, was used for computational learning. We employed the following data cleaning strategies: i) data were visually examined to ensure that all absorption bands were consistent with those reported in literature;[24,27,30–32] ii) principal component analysis (PCA) was employed for outliers detection, and the resulting hotelling's *T*-squared distribution (T^2) and leverage score were used to determine outliers; iii) all outliers were excluded while the rest of the dataset was passed on for modelling. Optimal preprocessing steps were determined via NIPPY python module.[33] Overall 50 NIPPY pipelines were explored, and preprocessed spectral corresponding to each donor were averaged before finally deployed for machine learning. For the train-test split methods, bones from different donors were used for training (13 patients) and for independent testing (seven patients).

The corresponding PLS-R score plots of the model (latent variable = 6) developed using the LOOCV (leave one out cross validation). Medians of the technical replicates acquired from each donor's sternal bone were used to avoid overfitting of models, thereby avoiding the 'technical replicate trap'. Classification analyses were performed via support vector machine (SVM) by considering the quartiles of the micro-CT parameters (Q1, Q2, Q3, and Q4) as the target variables. The best SVM-C models were determined using model metrics such as accuracy, precision, and recall, while PLS-R models were evaluated using the correlation coefficient (R^2), the root-mean-square error of cross validation (RMSECV), low root-mean square error of prediction (RMSEP), prediction bias, and calibration bias. An independent correlation using Spearman's rank correlation analysis was further used to show correlation between the Micro-CT parameters and predicted using NIR data.

Results

Fresh human bone for NIRS analysis. We obtained bone samples from 20 patients at a median age of 51 years (IQR 35 to 59), 12 (60%) of whom were male with a median BMI of 25.8 kg/m^2 (IQR 22.3 to 30.5). Further demographic and clinical details are outlined in Table I. The median bone volume, determined by micro-CT (Supplementary Figure b), was 17.97% (IQR 16.54 to 19.19), with other structural properties as outlined in Table I.

NIRS scans of bone. To assess the capacity of miniaturized NIRS to identify differences in bone quality, we compared the NIRS scans of bones from four different quartiles of bone volume fraction (BV/TV). We were able to undertake five NIRS scans in three seconds. Averaged NIR scans from each quartile of BV/TV (Figure 2) show key

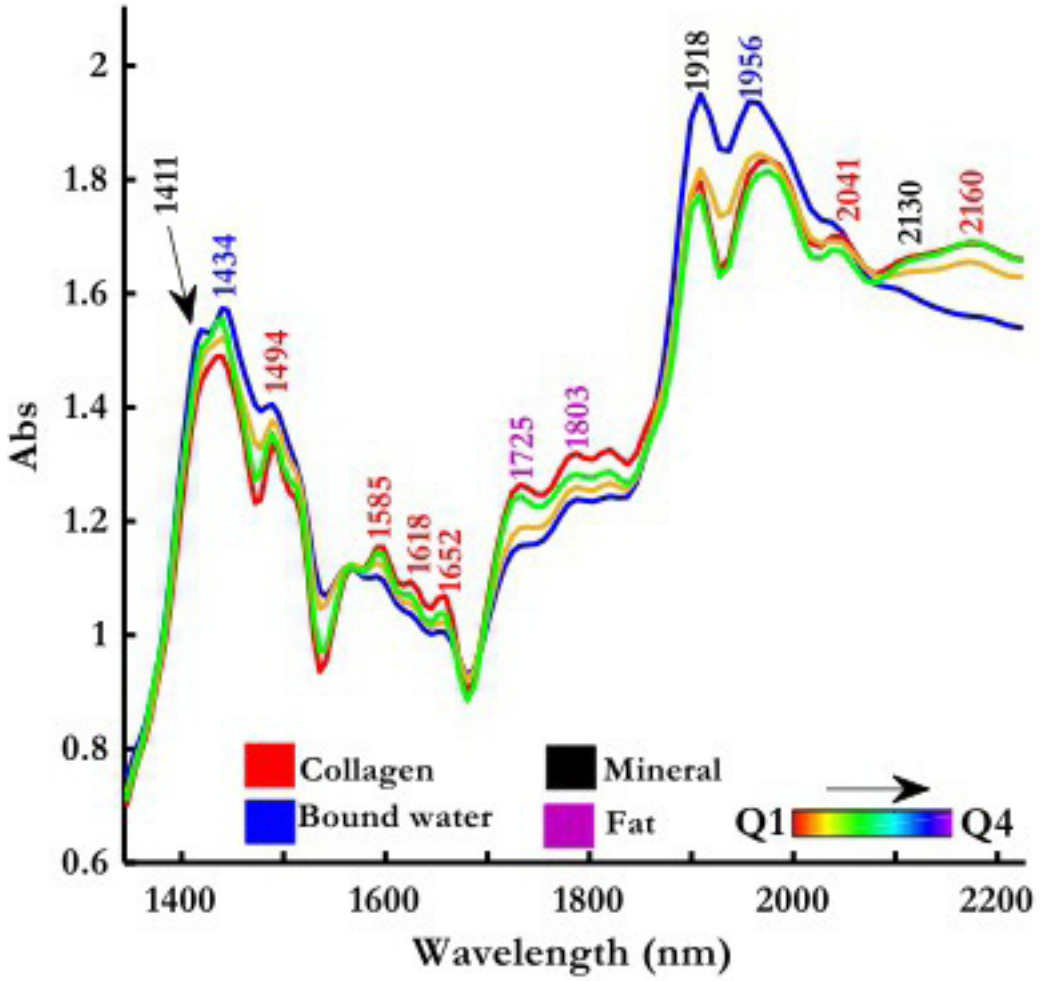

Fig. 2

Spectral differences in sternal bone of varying bone volume fraction and their band assignments: average near-infrared spectroscopy (NIR) spectra of human sternal bone recorded by a miniature NIR spectrometer with major bands labelled. The spectra revealed in vivo bone composition, mostly bound water, inorganic mineral content approximated as hydroxyapatite ($Ca_{10}(PO_4)_6(OH)_2$)), organic component (collagen), and bone marrow (fat/lipid). The spectra were presented based on the quartile ranking of the bone volume fraction (BV/TV) parameters. Red spectrum is Q1, green is Q2, yellow is Q3, and the blue spectrum depict Q4. Abs, absorbance, Q, quartile of bone volume fraction.

differences in absorption across wavelength ranges typically associated with collagen, minerals, lipid, and water (Figure 2). Patients with poorer quality bone (low BV/TV) were observed to have higher absorption at wavelengths associated with collagen (1,585, 1,618, and 1,652 nm),[34] bound water (1,438 nm and 1,956 nm),[24,27,30–32] and fat (1,725 nm and 1,803 nm),[30] with lower absorption at those related to minerals (1,411 nm and 1,918 nm).[35] These findings are consistent clinically, where patients with poorer-quality bone and lower BV/TV have a lower proportion of bone minerals, replaced with connective tissue such as collagen or fat.[34]

We also observed some physiological nuances of acquired NIR scans when compared to spectra of pure collagen and water. NIRS scans in this study are consistent with previous findings that show small peak shifts in physiological collagen and water compared to those in their pure state (Supplementary Figure c). For example, the peaks at 1,567, 1,694, and 2,178 nm in pure collagen spectrum (Supplementary Figure cb) can be observed to have shifted to 1,585, 1,652, and 2,160 nm in the bone spectra (Figure 2), which in the literature has been attributed to the structure of collagen in bone being different from the highly ordered nature of synthetic collagen.[36] OH vibrations naturally occurring around 1,450 nm and 1,935 nm in pure water (Supplementary Figure cc) can be observed to have shifted to 1,434 nm and 1,956 nm, respectively, indicative of interactions of water with bone matrix components ('bound water').[37]

Collectively, these findings demonstrate that NIR scans of fresh bones detects differences in bone quality (BV/TV), and they can be attributed to their absorption of collagen, minerals, water, and lipids. Further influence

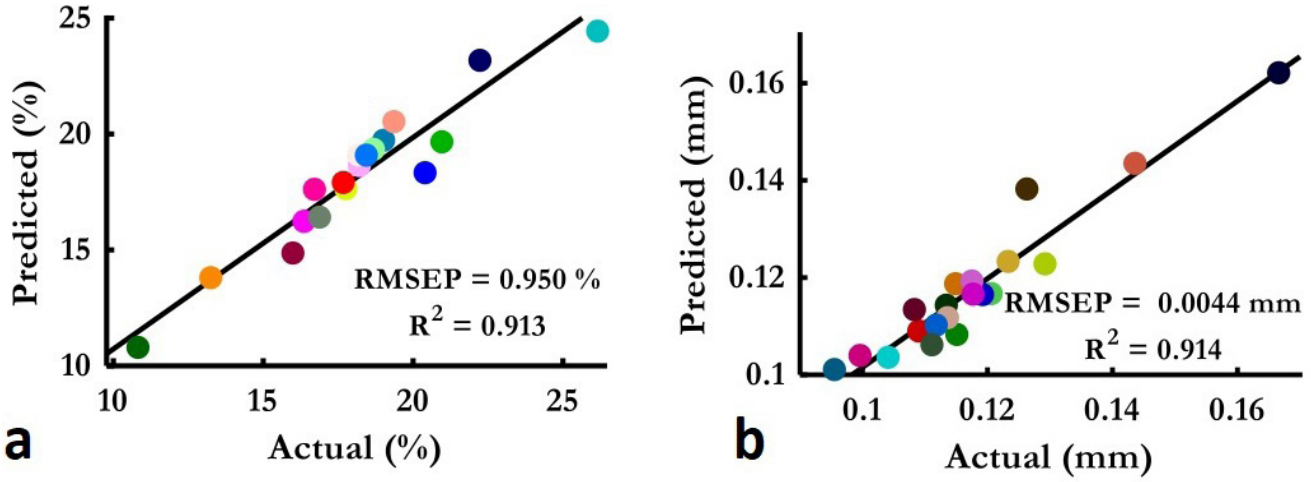

Fig. 3

Partial least square regression (PLS-R) analysis showing correlation between average near-infrared (NIR) spectra of human bone sample captured by miniature NIR spectrometer on the trabecular surface with the micro-CT parameters. The score plot shows the relationship between the measured spectral and a) bone volume fraction (BV/TV) and b) trabecular thickness (Tb.Th). RMSEP, root mean square error of prediction.

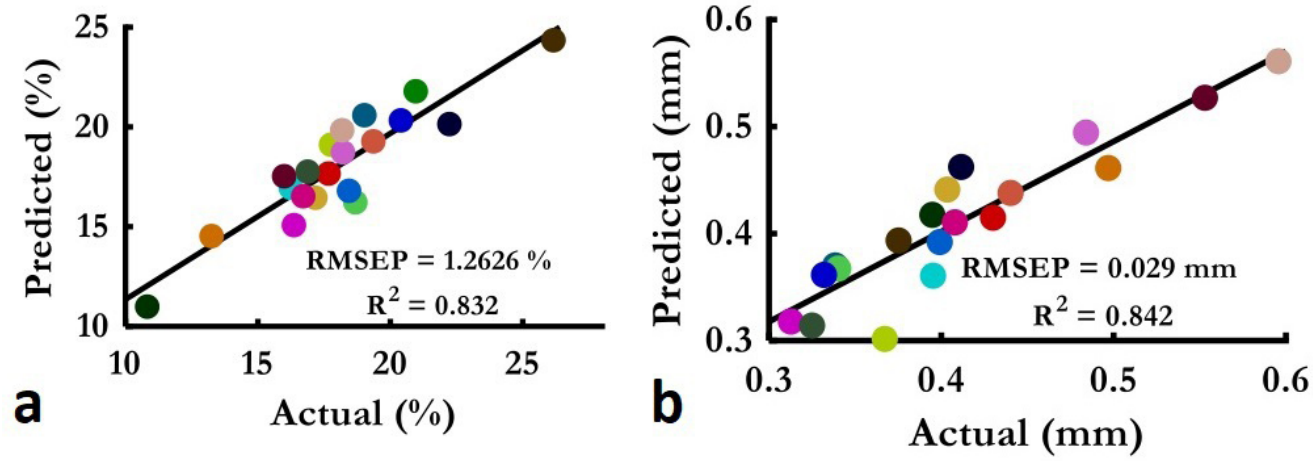

Fig. 4

Partial least square regression (PLS-R) analysis showing correlation between average near-infrared (NIR) spectra of a human bone sample acquired from the outer cortical surface, with the micro-CT parameters. The scores plot showed the relationship between the measured spectra and a) bone volume fraction and b) cortical thickness. RMSEP, root mean square error of prediction.

of mineral composition on the strength of correlation is explained in the Supplementary appendix.

Quantification of bone structure with NIRS. NIRS scans of the inner (trabecular) surface demonstrated excellent performance (Figure 3 and Supplementary Figure d) in predicting quality (BV/TV) with strong correlation and low error (R^2 = 0.913, and root mean square error of prediction, RMSEP = 0.95%) (Figure 3a). Similar performance was noted in predicting trabecular thickness (R^2 = 0.914) with a low margin of error (RMSEP = 0.0044 mm) (Figure 3b). Other trabecular properties also exhibited good performance (trabecular number R^2 = 0.88; trabecular spacing <*i*>*R*2 = 0.807) (Supplementary Figure d). Despite the cortical surface being at up to 1 cm from the probe surface in these measurements, good performance still obtained with cortical porosity (<*i*>*R*2 = 0.899) and cortical thickness (<*i*>*R*2 = 0.881) (Supplementary Figure d). The corresponding RMSEP, ratio product to deviation (RPD), and Spearman's rank analysis for Figures 4a to 4f are also shown in Table II.

When NIRS scans were taken from the cortical surface, we observed slightly lower performance in predictions of bone quality (BV/TV) (Figure 4a), but still with low margins of error (RMSEP = 1.26%). Promisingly, these measurements showed good performance for bone surface properties including cortical thickness (R^2 = 0.842) and porosity (<*i*>^{R}2 = 0.839) (Figure 4b). It also retained good performance in predicting deeper

Table II. Performance metrics for the partial least square regression models developed for both trabecular and cortical surfaces.

Variable	Ct.Po, %	Ct.Th, mm	Tb.N, mm^{-1}	Tb.Th, mm	Tb.Sp, mm	BV/TV, %
Predictions of structural characteristics from spectra taken at inner (trabecular) bone surface						
R^2	0.899	0.888	0.882	0.914	0.807	0.913
RMSECV	5.655	0.079	0.457	0.023	0.157	3.097
RMSEP	1.005	0.027	0.111	0.004	0.041	0.951
Prediction bias	5.4E-03	1.1E-04	1.0E-3	2.7E-5	1.5E-4	0.012
RPD	0.679	1.038	0.767	0.661	0.551	1.304
Spearman's rank	$p < 0.001$ for all measurements					
Spearman Rho	0.776	0.841	0.668	0.911	0.791	0.886
Predictions of structural characteristics from spectra taken at outer (cortical) bone surface						
R^2	0.839	0.899	0.782	0.793	0.808	0.833
RMSECV	6.021	0.231	0.293	0.037	0.096	4.852
RMSEP	1.323	0.030	0.145	0.007	0.041	1.263
Prediction bias	9.7E-03	2E-04	1.5E-3	4.9E-3	2.4E-3	7E-03
RPD	2.693	1.057	0.615	0.615	0.551	0.934
Spearman's rank	$p < 0.001$ for all measurements					
Spearman Rho	0.721	0.896	0.877	0.783	0.800	0.800

BV/TV, bone volume/total volume (bone volume fraction); Ct.Po, cortical porosit; Ct.Th, cortical thickness; RMSCEV, root square mean error of validation; RMSEP, Root mean square error of prediction; RPD, ratio of prediction to deviation; Tb.N, trabecular number; Tb.Sp, trabecular spacing; Tb.Th, trabecular thickness;

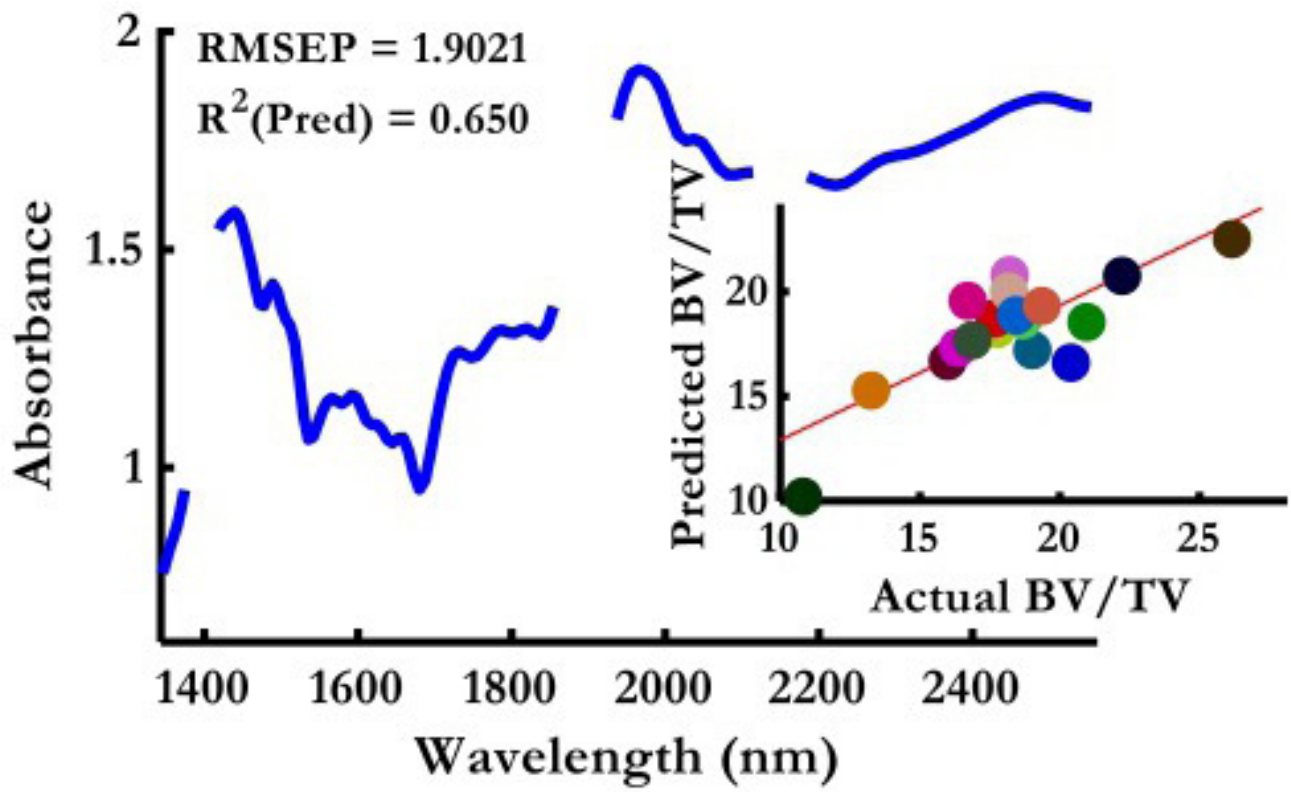

Fig. 5

Partial least square regression score plot after eliminating bones minerals absorption at region 1,411 nm and 2,130 nm. BV/TV, bone volume/total volume (bone volume fraction); RMSEP, root mean square error of prediction.

internal properties such as trabecular thickness (<$i^{>R}$2 = 0.792), spacing ($R2^{2=}$ 0.807), and number (<$i^{>R}$2 = 0.781) (Supplementary Figure e)

Influence of chemical composition on NIRS assessment. We assessed the influence of bone mineral (Figure 5), collagen (Figure 6), and fat (Supplementary Figure f) on the

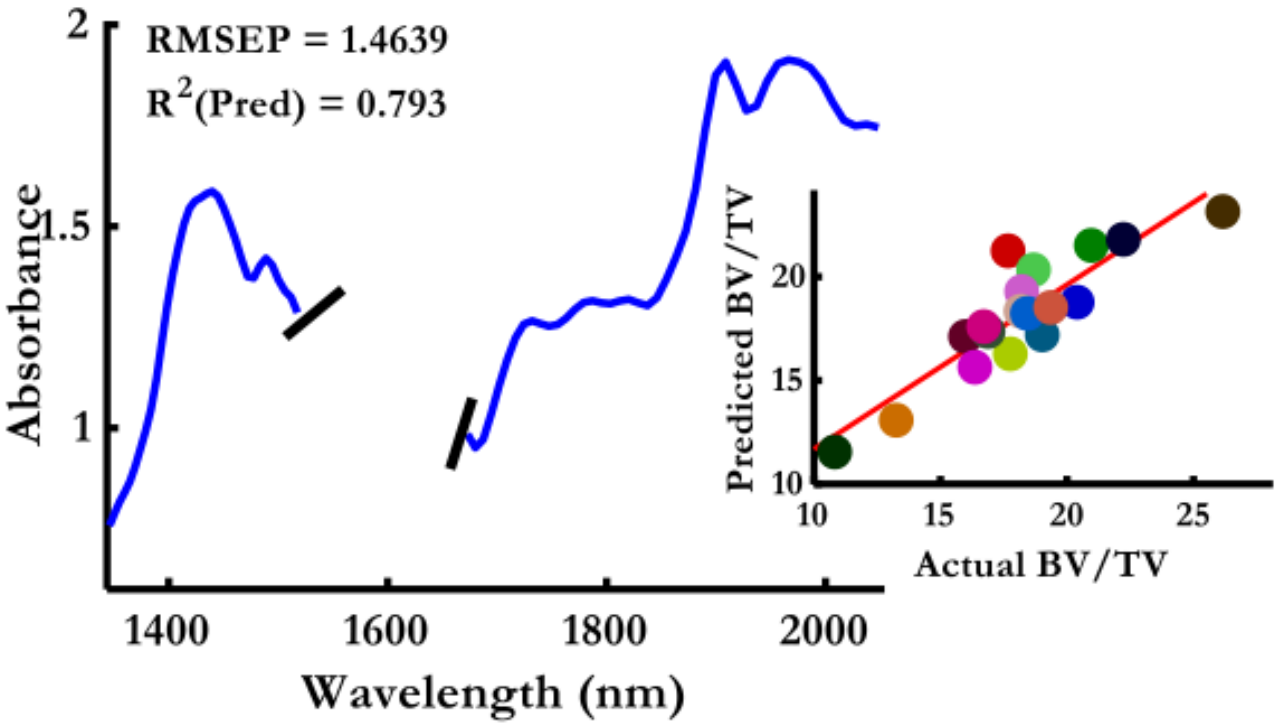

Fig. 6

Partial least square regression score plot after eliminating collagen modes at wavelength range 1,490 to 1,650 nm and 2,050 to 2,350 nm. BV/TV, bone volume/total volume (bone volume fraction); RMSEP, root mean square error of prediction.

performance of NIRS scans for predicting fresh bone quality. We omitted wavelengths associated with each component and assessed how altered the model performance (*R2* and RMSEP) for predicting bone volume fraction (BV/TV). By omitting bone marrow and fat (around 1,700 to 1,850 nm[30] (Supplementary Figure f)), there was only a marginal difference in model performance (<*i*>*R2* = 0.878 vs *R2* of full model = 0.913). Exclusion of spectral range indicative of bone minerals (Figure 5) had the most profound effect on model performance, with *R2* value decreasing to 0.65. Omission of collagen (combination of 2,050 to 2,350 nm and second overtone of 1,490 to 1,650 nm)[34,38] had a smaller influence on model performance (<*i*>*R2* = 0.793) (Figure 6). The loadings plot associated with these three models are presented in Supplementary Figure fd, depicting how the bands influenced each model. These findings demonstrate that the performance of NIRS scans critically rely on bone minerals and collagen but are less influenced by lipids.

Grading bone quality. We assessed the capacity of NIRS scans to predict the quartile of bone volume fraction (BV/TV) (Figures 7 and 8) and thickness (Ct.Th and Tb.Th) (Supplementary Figure g) using SVM classification and confusion matrices. For trabecular surface-based measurements, 100% classification accuracy was obtained for the upper three quartiles (Q2 to Q4) of bone quality but had 30% misclassification rate for low density bone (Q1 of BV/TV) (Figure 7). Classification accuracies of 100%, 80%, 100%, and 90% were obtained for the four quartiles, respectively, for Tb.Th (Supplementary Figure g). Measurements acquired from the outer (cortical) surface had 100% classification accuracy in predicting bone quality (BV/TV) (Figure 8) and surface thickness (Ct.Th) for all four quartiles (Supplementary Figure g).

Discussion

Currently, no intraoperative or live bone evaluation tools exist for human use. In this study we have demonstrated the capacity of NIRS scans, via a portable miniaturized spectrometer, to characterize fresh human sternal bone integrity in a noninvasive manner. This proof-of-concept study forms the first iterative step towards creating a non-destructive point-of-care tool for evaluating bone quality, with the following key results having implications for clinical practice. First, we demonstrated that NIRS scans can non-destructively quantify in depth microarchitectural properties of fresh human bone, including bone volume fraction, thickness, and porosity with scan times of less than three seconds. These properties can be used intraoperatively to tailor bone repair and/or selected the appropriate reconstruction technique. Second, we demonstrated that NIRS scans acquired from the surface

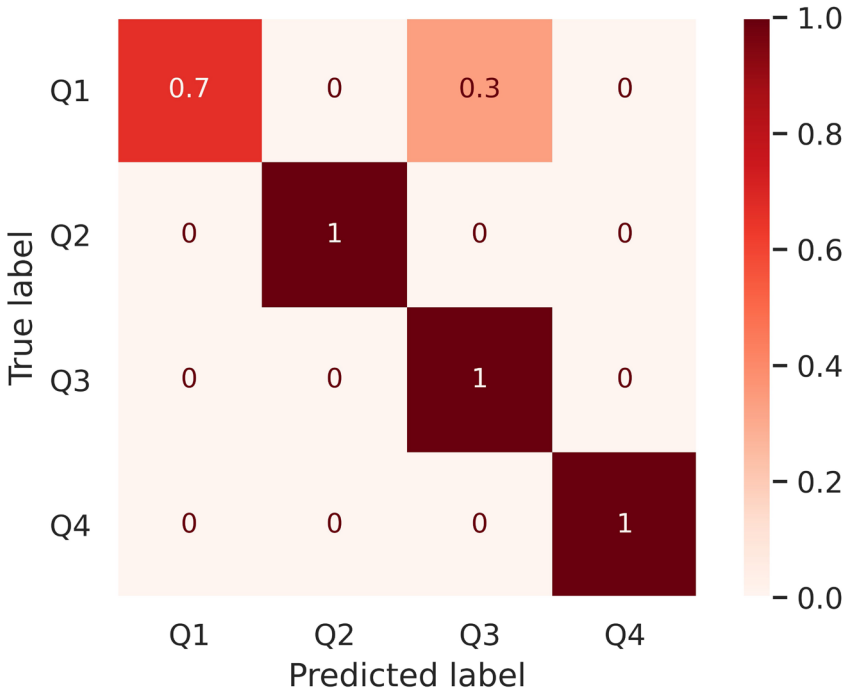

Fig. 7

Confusion matrix showing accuracy of predicting bone quality (bone volume fraction) using near-infrared spectroscopy scans taken at the trabecular surface.

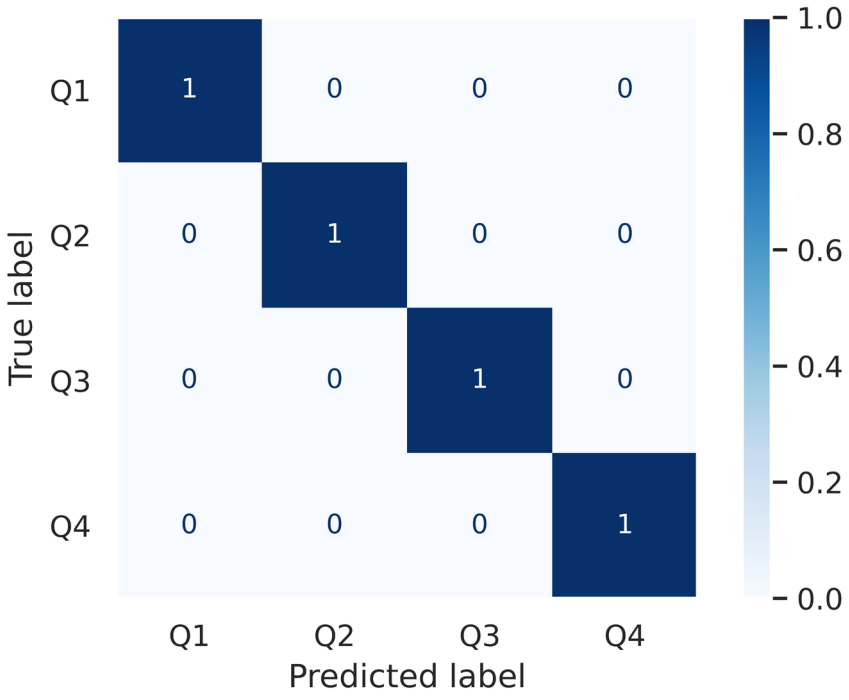

Fig. 8

Confusion matrix showing accuracy of predicting bone quality (bone volume fraction) using near-infrared spectroscopy scans taken at the cortical surface.

of bone can both quantify, with small margins of error, superficial properties (such as cortical thickness) and penetrate deep into the bone to accurately predict bone volume fraction. This suggests that the methodology can support intraoperative measurements to provide detailed assessment of underlying bone properties. Third, detailed assessment of the NIRS scans can provide insight into specific biochemical composition of bone (e.g. collagen, mineral, water, and fat content), allowing clinicians to assess not only structural properties but also changes

in biochemical composition due to disease. Fourth, we showed that NIRS scanning instrumentation has evolved to an extent where point-of-care use is possible, through a hand-held miniaturized spectrophotometer system, opening the possibilities for intraoperative use.

Our findings in fresh bone are consistent with previous literature in processed samples, which reported on a relationship between different wavelength ranges and predictive capabilities of subchondral bone properties from optical coherence tomography (OCT) parameters.[25] The prediction metrics, which decreased after accounting for the influence of bone marrow, bound water, mineralized matrix, and collagen moieties demonstrate the significance of whole bone scanning compared to previous report that only investigated bone mineral matrix.[31,32] Clinical translation of NIRS scans has been hindered by large and bulky benchtop laboratory-based instrumentation. A high level of computational processing and time-intensive chemometric analysis has traditionally been carried out sequentially with cumbersome equipment and delayed correlation using artificial intelligence techniques. Rapid advancement in process analytical technology, miniaturization, and computational learning have led to advancement in non-medical fields.[39] This study describes the first of many emerging clinical uses of NIRS, which include cancer,[40,41] serum markers,[24,41,42] heart disease,[43] transplant rejection,[44] and fibrosis.[45] In analyzing fresh human bone, our study marks a progression from studies where NIRS has been used to analyze animal and cadaveric human connective tissues,[24–27,46–49] or confined to prediction of bone water content.[30–32] While many of these studies are based on benchtop spectrophotometers, our report is one of the first to use portable and miniaturized handheld instrumentation to monitor disease using commercially available low-cost instruments in a non-destructive manner.[24] A key concern with instrument miniaturization is loss in the quality of scans. However, we demonstrate NIR scans to be highly resolved and show a high signal-to-noise ratio, making it possible to resolve the bands contributing to individual functional groups and clinical diagnoses. They are primarily based on absorption bands from protein (20%to 30%), bound water (10% to 20%), and bone matrix (50% to 60%). The smartphone or tablet user interface enables potential use as a mobile clinical instrument available to clinicians as point of care. The instrument is therefore capable of acquiring spectral measurements in clinical settings. Combined with rapid advances in machine-learning (ML), including well-defined guidelines outlining steps in developing clinical instruments for automated diagnoses,[50–52] it is our position that NIRS now bears the capability of being developed into an instrument for point-of-care use.

Clinically, these findings have the potential to help address the paucity of current techniques in assessing bone health. Morbidity from bone health is growing globally, and an ageing society with increasing prevalence of comorbidities such as diabetes, osteoporosis, and obesity accentuate its burden.[53–56] Bone health remains a very strong predictor of operative outcomes and recovery.[57–60] Our findings have potential for use in all bone surgery, but have immediate applications for median sternotomies, which remain the most common approach for cardiac surgery. The sternotomy is the most commonly performed osteotomy or bone-breaking surgery in the world. This is approximately linked to the global volume of surgically correctable heart disease. The majority of sternal closures are carried out with simple wires,[61] irrespective of bone health, and are fraught with increased morbidity from sternal wound breakdown from poorly individualized reconstruction.[62–64] An instrument that can assess bone health and guide a tailored intervention technique could significantly reduce this burden.[65,66] As these findings are consistent with bone and cartilage studies for other locations,[24–27,46–49] it is plausible that this technology could be extended to other orthopaedic or joint-related interventions.

The strengths of our work are as follows: this is the first study to use fresh-frozen human bone as opposed to previous studies that used human cadaveric bones, which have been processed in formaldehyde and stored for years.[30,31] The samples analyzed in this study are intraoperative samples analyzed in a non-destructive manner. They were not fixed or processed, and therefore represent a close emulation of intraoperative characteristics of the bone. Fixation has been shown to affect biological tissue constituents, alterating the physiological nature of tissue composition, resulting in assessment of the tissue in a non-physiological state. Moreover, NIRS scans are sensitive to fixing agents such as formalin which solidifies into paraformaldehyde, which may influence the resulting spectrum if the samples are not well processed and washed. We demonstrate that components historically eliminated by fixing tissues, such as marrow and bound water, improve the ability of NIR scans to predict structural properties of bone (Supplementary Figure i), further discussion of which can be found in our Supplementary Material.

Furthermore, although the samples in this study were obtained from a narrow distribution of population – median age 51 years (IQR 35 to 59), median cortical thickness 0.40 (IQR 0.35 to 0.46), and median bone volume fraction 17.97% (IQR 16.54% to 19.19%) – our approach still showed strong correlations ($R^2 > 0.80$) and small prediction errors (RMSCEV and RPD), with excellent classification accuracies using an array of advanced and robust ML techniques, including PLS and SVM. Given the narrow distribution of age and comorbidities of donor patients in this study, a more detailed study with larger sample sizes and variance would be needed before clinical

translation of our approach. We anticipate that with more data from a diverse range of patients in our ML algorithm, we will be able to clinically translate NIRS scans for assessment of sternal bone integrity. This could then be applied to other bones at the time of intervention.

Take home message

- We demonstrate that a handheld near-infrared spectroscopy instrument, which can obtain scans from tissue in under three seconds in a noninvasive matter, can accurately predict microstructural properties including bone volume fraction and thickness.
- We believe this is a fundamental step forward in creating an instrument capable of intraoperative real-time use.

Supplementary material

Additional influence analysis.

References

1. **Beveridge M**, **Howard A**. The burden of orthopaedic disease in developing countries. *J Bone Joint Surg Am*. 2004;86-A(8):1819–1822.
2. **Yelin E**, **Weinstein S**, **King T**. The burden of musculoskeletal diseases in the United States. *Semin Arthritis Rheum*. 2016;46(3):259–260.
3. **Raman J**, **Song DH**, **Bolotin G**, **Jeevanandam V**. Sternal closure with titanium plate fixation--a paradigm shift in preventing mediastinitis. *Interact Cardiovasc Thorac Surg*. 2006;5(4):336–339.
4. **Chiang H-Y**, **Kamath AS**, **Pottinger JM**, **et al**. Risk factors and outcomes associated with surgical site infections after craniotomy or craniectomy. *J Neurosurg*. 2014;120(2):509–521.
5. **de Moya M**, **Nirula R**, **Biffl W**. Rib fixation: Who, what, when? *Trauma Surg Acute Care Open*. 2017;2(1):e000059.
6. **Elsalanty ME**, **Genecov DG**. Bone grafts in craniofacial surgery. *Craniomaxillofac Trauma Reconstr*. 2009;2(3):125–134.
7. **Dean NR**, **White HN**, **Carter DS**, **et al**. Outcomes following temporal bone resection. *Laryngoscope*. 2010;120(8):1516–1522.
8. **Coughlin TR**, **Romero-Moreno R**, **Mason DE**, **et al**. Bone: A fertile soil for cancer metastasis. *Curr Drug Targets*. 2017;18(11):1281–1295.
9. **Kneser U**, **Schaefer DJ**, **Polykandriotis E**, **Horch RE**. Tissue engineering of bone: the reconstructive surgeon's point of view. *J Cell Mol Med*. 2006;10(1):7–19.
10. **Cohen B**, **Rushton N**. Accuracy of DEXA measurement of bone mineral density after total hip arthroplasty. *J Bone Joint Surg Br*. 1995;77-B(3):479–483.
11. **Tempel ZJ**, **Gandhoke GS**, **Okonkwo DO**, **Kanter AS**. Impaired bone mineral density as a predictor of graft subsidence following minimally invasive transpsoas lateral lumbar interbody fusion. *Eur Spine J*. 2015;24 Suppl 3:414–419.
12. **Choksi P**, **Jepsen KJ**, **Clines GA**. The challenges of diagnosing osteoporosis and the limitations of currently available tools. *Clin Diabetes Endocrinol*. 2018;4:12.
13. **Deckelmann S**, **Schwyn R**, **Van der Pol B**, **Windolf M**, **Heini PF**, **Benneker LM**. DensiProbe Spine: A novel instrument for intraoperative measurement of bone density in transpedicular screw fixation. *Spine (Phila Pa 1976)*. 2010;35(6):607–612.
14. **Klotz MCM**, **Beckmann NA**, **Bitsch RG**, **Seebach E**, **Reiner T**, **Jäger S**. Bone quality assessment for total hip arthroplasty with intraoperative trabecular torque measurements. *J Orthop Surg Res*. 2014;9:109.
15. **Féron JM**, **Mauprivez R**. Fracture repair: general aspects and influence of osteoporosis and anti-osteoporosis treatment. *Injury*. 2016;47 Suppl 1:S10–4.
16. **Fonseca H**, **Moreira-Gonçalves D**, **Coriolano H-JA**, **Duarte JA**. Bone quality: the determinants of bone strength and fragility. *Sports Med*. 2014;44(1):37–53.
17. **Spross C**, **Zeledon R**, **Zdravkovic V**, **Jost B**. How bone quality may influence intraoperative and early postoperative problems after angular stable open reduction-internal fixation of proximal humeral fractures. *J Shoulder Elbow Surg*. 2017;26(9):1566–1572.
18. **Ridderstolpe L**, **Gill H**, **Granfeldt H**, **Ahlfeldt H**, **Rutberg H**. Superficial and deep sternal wound complications: incidence, risk factors and mortality. *Eur J Cardiothorac Surg*. 2001;20(6):1168–1175.
19. **Donnelly E**, **Boskey AL**, **Baker SP**, **van der Meulen MCH**. Effects of tissue age on bone tissue material composition and nanomechanical properties in the rat cortex. *J Biomed Mater Res A*. 2010;92(3):1048–1056.
20. **Unal M**, **Ahmed R**, **Mahadevan-Jansen A**, **Nyman JS**. Compositional assessment of bone by Raman spectroscopy. *Analyst*. 2021;146(24):7464–7490.
21. **Spizzirri PG**, **Cochrane NJ**, **Prawer S**, **Reynolds EC**. A comparative study of carbonate determination in human teeth using Raman spectroscopy. *Caries Res*. 2012;46(4):353–360.
22. **Uppuganti S**, **Granke M**, **Makowski AJ**, **Does MD**, **Nyman JS**. Age-related changes in the fracture resistance of male Fischer F344 rat bone. *Bone*. 2016;83:220–232.
23. **Adegoke JA**, **De Paoli A**, **Afara IO**, **et al**. Ultraviolet/visible and near-infrared dual spectroscopic method for detection and quantification of low-level malaria parasitemia in whole blood. *Anal Chem*. 2021;93(39):13302–13310.
24. **Adegoke JA**, **Kochan K**, **Heraud P**, **Wood BR**. A near-infrared "matchbox size" spectrometer to detect and quantify malaria parasitemia. *Anal Chem*. 2021;93(13):5451–5458.
25. **Afara IO**, **Florea C**, **Olumegbon IA**, **et al**. Characterizing human subchondral bone properties using near-infrared (NIR) spectroscopy. *Sci Rep*. 2018;8(1):9733.
26. **Nippolainen E**, **Shaikh R**, **Virtanen V**, **et al**. Near infrared spectroscopy enables differentiation of mechanically and enzymatically induced cartilage injuries. *Ann Biomed Eng*. 2020;48(9):2343–2353.
27. **Afara IO**, **Sarin JK**, **Ojanen S**, **et al**. Machine learning classification of articular cartilage integrity using near infrared spectroscopy. *Cell Mol Bioeng*. 2020;13(3):219–228.
28. **Campbell GM**, **Sophocleous A**. Quantitative analysis of bone and soft tissue by micro-computed tomography: applications to ex vivo and in vivo studies. *Bonekey Rep*. 2014;3:564.
29. **Shim J**, **Iwaya C**, **Ambrose CG**, **Suzuki A**, **Iwata J**. Micro-computed tomography assessment of bone structure in aging mice. *Sci Rep*. 2022;12(1):8117.
30. **Rajapakse CS**, **Padalkar MV**, **Yang HJ**, **Ispiryan M**, **Pleshko N**. Non-destructive NIR spectral imaging assessment of bone water: Comparison to MRI measurements. *Bone*. 2017;103:116–124.
31. **Ailavajhala R**, **Querido W**, **Rajapakse CS**, **Pleshko N**. Near infrared spectroscopic assessment of loosely and tightly bound cortical bone water. *Analyst*. 2020;145(10):3713–3724.
32. **Ailavajhala R**, **Oswald J**, **Rajapakse CS**, **Pleshko N**. Environmentally-controlled near infrared spectroscopic imaging of bone water. *Sci Rep*. 2019;9(1):10199.
33. **Torniainen J**, **Afara IO**, **Prakash M**, **Sarin JK**, **Stenroth L**, **Töyräs J**. Open-source python module for automated preprocessing of near infrared spectroscopic data. *Anal Chim Acta*. 2020;1108:1–9.
34. **Workman J**, **Weyer L**. *Practical Guide to Interpretive Near-Infrared Spectroscopy*. 2007: CRC Press, Inc.
35. **Kolmas J**, **Marek D**, **Kolodziejski W**. Near-infrared (NIR) spectroscopy of synthetic hydroxyapatites and human dental tissues. *Appl Spectrosc*. 2015;69(8):902–912.
36. **Bakir G**, **Girouard BE**, **Wiens R**, **et al**. Orientation matters: Polarization dependent IR spectroscopy of collagen from intact tendon down to the single fibril level. *Molecules*. 2020;25(18):18.
37. **Padalkar MV**, **Pleshko N**. Wavelength-dependent penetration depth of near infrared radiation into cartilage. *Analyst*. 2015;140(7):2093–2100.
38. **Baykal D**, **Irrechukwu O**, **Lin P-C**, **Fritton K**, **Spencer RG**, **Pleshko N**. Nondestructive assessment of engineered cartilage constructs using near-infrared spectroscopy. *Appl Spectrosc*. 2010;64(10):1160–1166.
39. **Pasquini C**. Near infrared spectroscopy: A mature analytical technique with new perspectives - A review. *Anal Chim Acta*. 2018;1026:8–36.
40. **Kondepati VR**, **Heise HM**, **Backhaus J**. Recent applications of near-infrared spectroscopy in cancer diagnosis and therapy. *Anal Bioanal Chem*. 2008;390(1):125–139.
41. **Pal UM**, **Gk AV**, **Gogoi G**, **et al**. Towards a portable platform integrated with multispectral noncontact probes for delineating normal and breast cancer tissue based on near-infrared spectroscopy. *IEEE Trans Biomed Circuits Syst*. 2020;14(4):879–888.
42. **Beć KB**, **Grabska J**, **Huck CW**. Near-infrared spectroscopy in bio-applications. *Molecules*. 2020;25(12):2948.
43. **Waksman R**, **Di Mario C**, **Torguson R**, **et al**. Identification of patients and plaques vulnerable to future coronary events with near-infrared spectroscopy intravascular ultrasound imaging: a prospective, cohort study. *Lancet*. 2019;394(10209):1629–1637.
44. **Tiwari S**, **Reddy VB**, **Bhargava R**, **Raman J**. Computational chemical imaging for cardiovascular pathology: chemical microscopic imaging accurately determines cardiac transplant rejection. *PLoS One*. 2015;10(5):e0125183.
45. **Zimmermann E**, **Mukherjee SS**, **Falahkheirkhah K**, **et al**. Detection and quantification of myocardial fibrosis using stain-free infrared spectroscopic imaging. *Arch Pathol Lab Med*. 2021;145(12):1526–1535.

46. **Afara I**, **Prasadam I**, **Crawford R**, **Xiao Y**, **Oloyede A**. Non-destructive evaluation of articular cartilage defects using near-infrared (NIR) spectroscopy in osteoarthritic rat models and its direct relation to Mankin score. *Osteoarthritis Cartilage*. 2012;20(11):1367–1373.
47. **Ala-Myllymäki J**, **Paakkonen T**, **Joukainen A**, **et al**. Near-infrared spectroscopy for mapping of human meniscus biochemical constituents. *Ann Biomed Eng*. 2021;49(1):469–476.
48. **Martínez Cortizas A**, **López-Costas O**. Linking structural and compositional changes in archaeological human bone collagen: an FTIR-ATR approach. *Sci Rep*. 2020;10(1):17888.
49. **Power AC**, **Chapmanb J**, **Cozzolinoc D**. Near infrared spectroscopy, the skeleton key for bone identification. Spectroscopy Europe. 2018;30(6):19–21.
50. **Mirbabaie M**, **Stieglitz S**, **Frick NRJ**. Artificial intelligence in disease diagnostics: a critical review and classification on the current state of research guiding future direction. *Health Technol*. 2021;11(4):693–731.
51. **Dey D**, **Slomka PJ**, **Leeson P**, **et al**. Artificial Intelligence in Cardiovascular Imaging. *Journal of the American College of Cardiology*. 2019;73(11):1317–1335.
52. **No authors listed**. Machine-learning workflow. 2022. https://cloud.google.com/ai-platform/docs/ml-solutions-overview (date last accessed 2 March 2023).
53. **Gehweiler D**, **Styger U**, **Gueorguiev B**, **Colcuc C**, **Vordemvenne T**, **Wähnert D**. Local bone quality measure and construct failure prediction: a biomechanical study on distal femur fractures. *Arch Orthop Trauma Surg*. 2022;142(6):1055–1061.
54. **Hoppe S**, **Uhlmann M**, **Schwyn R**, **Suhm N**, **Benneker LM**. Intraoperative mechanical measurement of bone quality with the DensiProbe. *J Clin Densitom*. 2015;18(1):109–116.
55. **Huang C-C**, **Jiang C-C**, **Hsieh C-H**, **Tsai C-J**, **Chiang H**. Local bone quality affects the outcome of prosthetic total knee arthroplasty. *J Orthop Res*. 2016;34(2):240–248.
56. **McAndrew CM**, **Agarwalla A**, **Abraham AC**, **Feuchtbaum E**, **Ricci WM**, **Tang SY**. Local bone quality measurements correlates with maximum screw torque at the femoral diaphysis. *Clin Biomech (Bristol, Avon)*. 2018;52:95–99.
57. **Alliston T**. Biological regulation of bone quality. *Curr Osteoporos Rep*. 2014;12(3):366–375.
58. **Aro HT**. Bone quality makes a difference. *Acta Orthop*. 2021;92(5):503–504.
59. **Saito M**, **Marumo K**. (New methods for the evaluation of bone quality. How does decay bone quality?). *Clin Calcium*. 2017;27(8):1075–1087. (Article in Japanese).
60. **Unnanuntana A**, **Rebolledo BJ**, **Khair MM**, **DiCarlo EF**, **Lane JM**. Diseases affecting bone quality: beyond osteoporosis. *Clin Orthop Relat Res*. 2011;469(8):2194–2206.
61. **Çiçek S**. Sternal closure: Wires are still the king! *J Thorac Cardiovasc Surg*. 2018;156(4):1596–1597.
62. **Singh K**, **Anderson E**, **Harper JG**. Overview and management of sternal wound infection. *Semin Plast Surg*. 2011;25(1):25–33.
63. **Tang GHL**, **Maganti M**, **Weisel RD**, **Borger MA**. Prevention and management of deep sternal wound infection. *Semin Thorac Cardiovasc Surg*. 2004;16(1):62–69.
64. **Group TPMS**. Risk factors for deep sternal wound infection after sternotomy: a prospective, multicenter study. *J Thorac Cardiovasc Surg*. 1996;111(6):1200–1207.
65. **Raman J**, **Lehmann S**, **Zehr K**, **et al**. Sternal closure with rigid plate fixation versus wire closure: a randomized controlled multicenter trial. *Ann Thorac Surg*. 2012;94(6):1854–1861.
66. **Engelman DT**, **Ben Ali W**, **Williams JB**, **et al**. Guidelines for perioperative care in cardiac surgery: Enhanced recovery after surgery society recommendations. *JAMA Surg*. 2019;154(8):755–766.

Author information:
- V. J. Sharma, MBBS, MPH, Cardiothoracic Surgery Trainee
- J. Raman, MBBS, MMed, PhD, FRACS, Professor and Cardiothoracic Surgeon
  Department of Surgery, Melbourne Medical School, University of Melbourne, Melbourne, Australia; Brian F. Buxton Department of Cardiac and Thoracic Aortic Surgery, Austin Hospital, Melbourne, Australia; Spectromix Laboratory, Melbourne, Australia.
- J. A. Adegoke, PhD, Research Fellow
- B. R. Wood, PhD, Professor and Laboratory Head
  Spectromix Laboratory, Melbourne, Australia; Centre for Biospectroscopy, Monash University, Melbourne, Australia.
- I. O. Afara, PhD, Associate Professor and Senior Research Fellow, Spectromix Laboratory, Melbourne, Australia; Centre for Biospectroscopy, Monash University, Melbourne, Australia; Biomedical Spectroscopy Laboratory, Department of Applied Physics, University of Eastern Finland, Kuopio, Finland; School of Information Technology and Electrical Engineering Faculty of Engineering, Architecture and Information Technology, Melbourne, Australia.
- K. Stok, PhD, Associate Professor, Department of Biomedical Engineering, University of Melbourne, Melbourne, Australia.
- E. Poon, PhD, Research Fellow, Spectromix Laboratory, Melbourne, Australia; Department of Medicine, Melbourne Medical School, University of Melbourne, Melbourne, Australia.
- C. L. Gordon, MBBS, MA, PhD, FRACP, Infectious Disease Physician, Immunologist, and Senior Research Fellow, Department of Medicine, Melbourne Medical School, University of Melbourne, Melbourne, Australia; Department of Infectious Diseases, Austin Hospital, Melbourne, Australia.

Author contributions:
- V. J. Sharma: Conceptualization, Investigation, Formal analysis, Writing – original draft, Writing – review & editing.
- J. A. Adegoke: Conceptualization, Investigation, Formal analysis, Writing – original draft, Writing – review & editing.
- I. O. Afara: Conceptualization, Investigation, Formal analysis, Writing – original draft, Writing – review & editing.
- K. Stok: Formal analysis, Writing – original draft, Writing – review & editing.
- E. Poon: Conceptualization, Investigation, Formal analysis, Writing – original draft, Writing – review & editing.
- C. L. Gordon: Investigation, Writing – review & editing.
- B. R. Wood: Conceptualization, Investigation, Formal analysis, Writing – original draft, Writing – review & editing.
- J. Raman: Conceptualization, Investigation, Formal analysis, Writing – original draft, Writing – review & editing.

- V. J. Sharma and J. A. Adegoke are joint first authors.

- B. R. Wood and J. Raman are joint senior authors.

Funding statement:
- The authors received no financial or material support for the research, authorship, and/or publication of this article.

ICMJE COI statement:
- K. Stok reports payment for participation on the RegMed XB Moonshot International Scientific Advisory Board, unrelated to this study. K. Stok is also an executive committee member of OCTA Research, the co-chair of SPECTRA, and a member of the ARC College of Experts.

Acknowledgements:
- The data that support the findings of this study are available on request from the corresponding author. The data are not publicly available due to privacy or ethical restrictions.

Ethical review statement:
- This study was approved by the Human Resources and Ethics committee (HREC) at Austin Hospital, Heidelberg, Melbourne, Victoria (HREC/73660/Austin-2021).

Open access funding:
- The authors confirm the open access fee for this study was self-funded.